Supplementary Information for

Boosting Fast and Stable Sodium-Ion Storage in TiO_2 by Amorphization Engineering and Superstructure Design

Xuanyu Lyu,[a] Ziyue Zheng,[b] Jiaoying Xie,[a] Jing Yang,[b] Dong Yang,[a] Yajun Wang,[*c] Tongtao Li,[*b] and Angang Dong[*b]

[a.] *State Key Laboratory of Molecular Engineering of Polymers and Department of Macromolecular Science, Fudan University, Shanghai 200433, China.*

[b.] *State Key Laboratory of Porous Materials for Separation and Conversion and Department of Chemistry, Shanghai Key Laboratory of Molecular Catalysis and Innovative Materials, and iChEM, Fudan University, Shanghai 200433, China.*

[c.] *College of Chemistry and Materials Engineering, Wenzhou University, Wenzhou 325027, China.*

Experimental Section

Materials

Oleic acid (OA), oleylamine (OAm), tris(hydroxymethyl)aminomethane, and dopamine hydrochloride were purchased from Aladdin. Hydrofluoric acid (HF) and hydrochloric acid (HCl) were purchased from Sinopharm Chemical Reagent Co. Ltd (China). Ti_2AlC powders were purchased from 11Technology Co., Ltd., Jilin, China. CNT powders were purchased from Qingdao Haoxin Co., Ltd. $Na_3V_2(PO_4)_3$ powders were purchased from Duoduochem Co., Ltd Suzhou, China.

Preparation of am-TiO_2 NSs:

The am-TiO_2 NSs were synthesized via a topochemical transformation process of Ti_2CT_x MXene nanosheets in a nonpolar solvent.[1] Initially, pristine Ti_2CT_x NSs were synthesized through selective etching of Ti_2AlC powders (0.5 g) in 20 mL aqueous mixture of HF (2 mL, 40 wt%) and HCl (12 mL, 12M) followed by a liquid-exfoliation process.[2] Subsequently, the resulting monolayer Ti_2CT_x NSs were functionalized with OAm and OA ligands and underwent natural oxidation in a $CHCl_3$ solution. The resulting am-TiO_2 NSs were purified through ethanol washing to remove residual ligands and then redispersed in $CHCl_3$ at a concentration of 60 mg/mL for subsequent use.

Surface-modification of CNTs:

The surface modification of CNTs involves a two-step procedure. Initially, pristine CNTs underwent functionalization with poly(dopamine) to introduce additional functional groups onto the surface. Subsequently, the pre-treated CNTs were further functionalized with OAm and OA ligands. In a typical process, 200 mg of CNTs were dispersed in a solution comprising ethanol (100 mL) and water (80 mL) through sonication for 1 h. Subsequently, 400 mg of dopamine was introduced into the solution, followed by the addition of 200 mL of an aqueous TRIS solution (600 mg). The resultant mixture was stirred for 24 h at room temperature. The resulting product (donated as CNT-PDA) was collected by filtration, washed with ethanol and water, and subsequently dried in a vacuum oven at 80 °C for 12 h.[3]

In the second step, the obtained CNT-PDA powders (200 mg) were added to a mixed solution consisting of 50 mL of $CHCl_3$, 5 mL of OAm, and 5 mL of OA under sonication for 2 h. The ligand-modified CNTs (CNT-OAm,OA) were subjected to ethanol washing for purification, and then redispersed in $CHCl_3$ at a concentration of 10 mg/mL.

Fabrication of am-TiO_2-CNT, c-TiO_2, and ca-TiO_2-CNT.

The co-assembly of am-TiO_2 NSs and ligand-modified CNTs was induced through a solvent evaporation process. Briefly, a $CHCl_3$ solution containing am-TiO_2 nanosheets and as-prepared ligand-grafted CNTs, with a mass ratio of 5:1, was allowed to evaporate under ambient conditions within a container. The complete solvent evaporation leads to the formation of lamellar superstructures in which CNTs are intercalated into the interlayers of stacked am-TiO_2 NSs. To carbonize the ligands, the as-assembled superstructures were subjected to thermal treatment at 500°C under an argon atmosphere for 2 h, resulting in the formation of am-TiO_2-CNT. The content of am-TiO_2 NSs in am-TiO_2-CNT was 65-75 wt%, depending on the ratio of the two components used for co-assembly.

The synthesis of c-TiO_2 NPs followed a similar procedure, albeit without the addition of ligand-grafted CNTs during self-assembly. The ca-TiO_2-CNT and c-TiO_2-CNT were obtained by mixing the commercial TiO_2 powders and c-TiO_2 NPs with CNT powders with a mass ratio of 5:1.

Materials characterization

Transmission electron microscopy (TEM) images, high-resolution TEM (HRTEM) images, high-angle annular dark-field scanning TEM (HAADF-STEM) images, and energy dispersive X-ray spectroscopy (EDS) were carried out on a Tecnai G2 F20 S-Twin microscope operated at 200 kV. Scanning electron microscopy (SEM) images were obtained using a Zeiss Ultra-55 microscope operated at 3 kV. The electrical conductivities were characterized by a four-point probe instrument (SB118, Shanghai Qianfeng Electronic Instrument Co., Ltd, China). X-ray diffraction (XRD) measurements were carried out on a Bruker D4 Xray diffractometer. Raman spectra

were obtained at room temperature on a XploRA Raman system. Fourier-transform infrared (FTIR) spectra were collected by a PerkinElmer Spectrum Two spectrometer. X-ray photoelectron spectroscopy (XPS) was conducted on a Perkin Elmer PHI-5000C ECSA system. N_2 adsorption-desorption isotherms were collected by a Quadrasorb evo H1101416. The contact angle measurements with the electrolytes were carried out on a DSA-25 drop shape analyzer at room temperature.

Electrochemical Measurements

CR2016-type coin cells were assembled in a glove box with H_2O and O_2 levels maintained below 0.1 ppm to evaluate the electrochemical performances of TiO_2-based materials. The working electrodes comprised as-synthesized active materials, Super P, and polyvinylidene difluoride (PVDF) in a mass ratio of 8:1:1, with an average mass loading of ~1.0 mg/cm^2. Sodium disks served as the counter electrodes, while glass fiber films were used as separators. The electrolyte for sodium-ion batteries (SIBs) consisted of 1 M $NaPF_6$ in pure diglyme. Cyclic voltammetry (CV) and electrochemical impedance spectroscopy (EIS) were conducted using a CHI660D electrochemical workstation. Galvanostatic measurements and galvanostatic intermittent titration technique (GITT) measurements were carried out on a Land CT2001A cell test system.

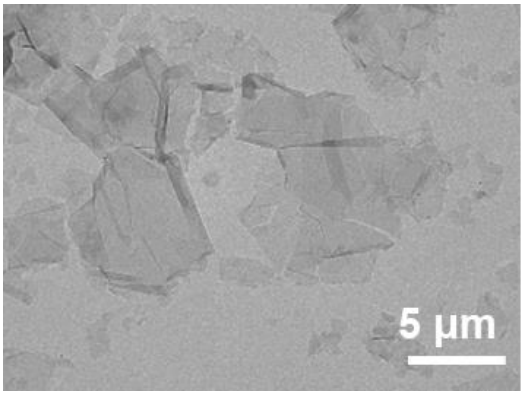

Fig. S1. Typical TEM image of colloidal am-TiO_2 NSs.

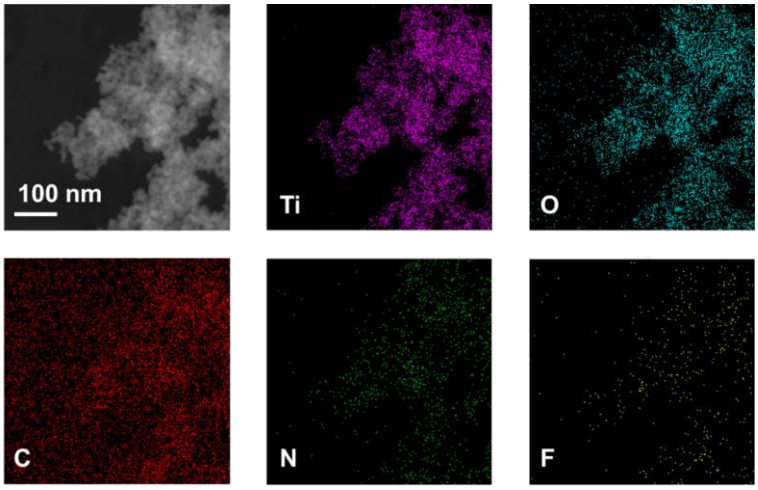

Fig. S2. STEM image and corresponding elemental mappings of c-TiO_2 NPs.

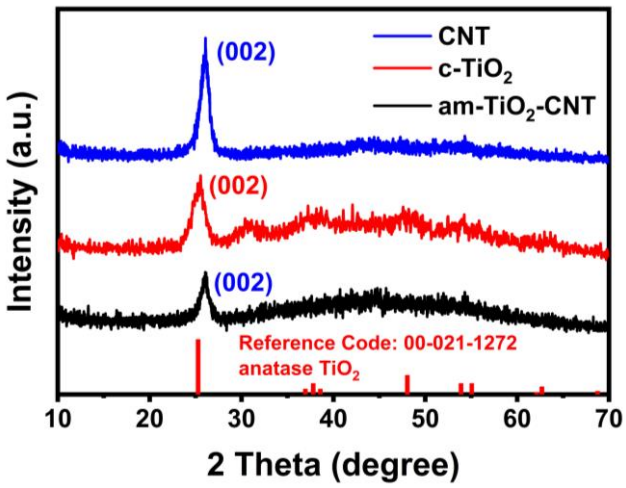

Fig. S3. XRD patterns of c-TiO_2 NPs, am-TiO_2-CNT, and CNT powders, respectively. The (002) peak in the XRD pattern of am-TiO_2-CNT originated from CNTs, while the absence of the anatase TiO_2 peaks suggested the amorphous nature of TiO_2 in am-TiO_2-CNT.

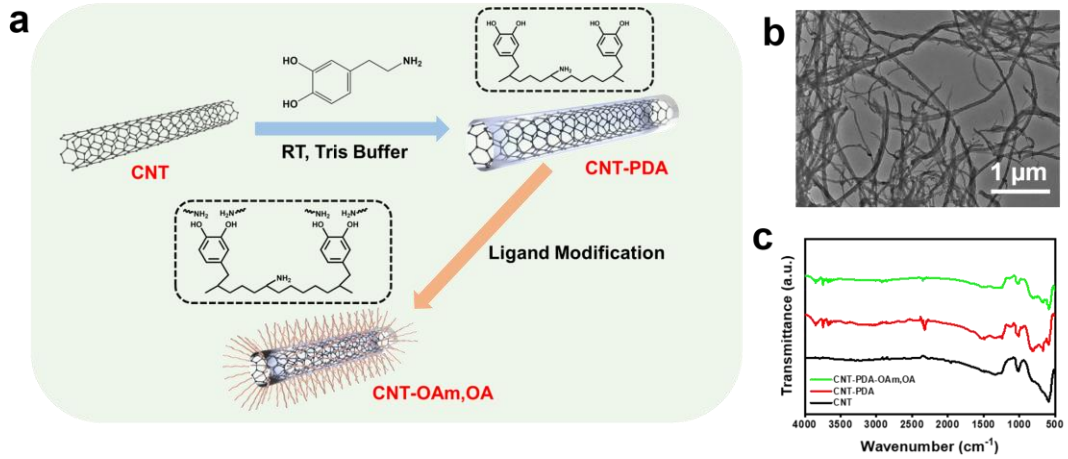

Fig. S4. (a). Schematic illustration of surface modification of CNTs. (b). TEM image of pristine CNTs. (c) FTTR spectra of CNTs, CNT-PDA and CNT-OAm,OA.

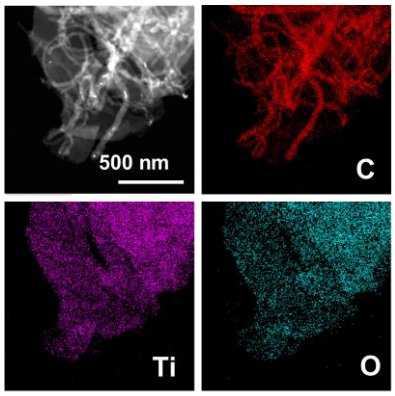

Fig. S5. STEM image and corresponding elemental mappings of am-TiO_2-CNT.

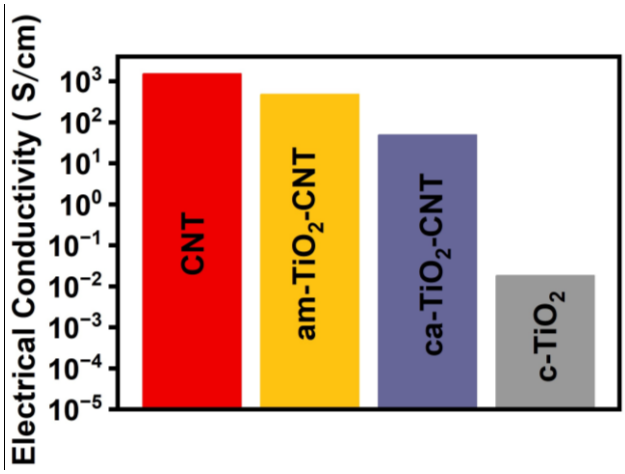

Fig. S6. Electrical conductivity of pristine CNTs, am-TiO_2-CNT, ca-TiO_2-CNT, and c-TiO_2 NPs. The CNT content in am-TiO_2-CNT and ca-TiO_2-CNT was the same.

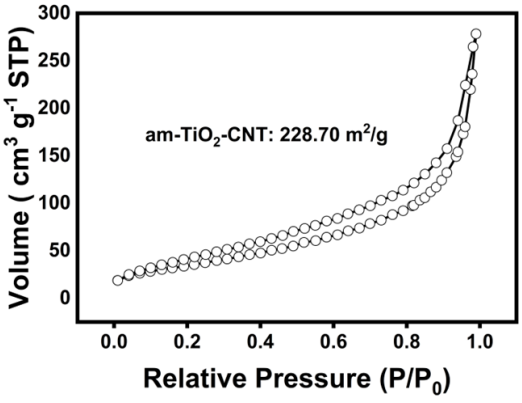

Fig. S7. N_2 adsorption-desorption isotherm of am-TiO_2-CNT.

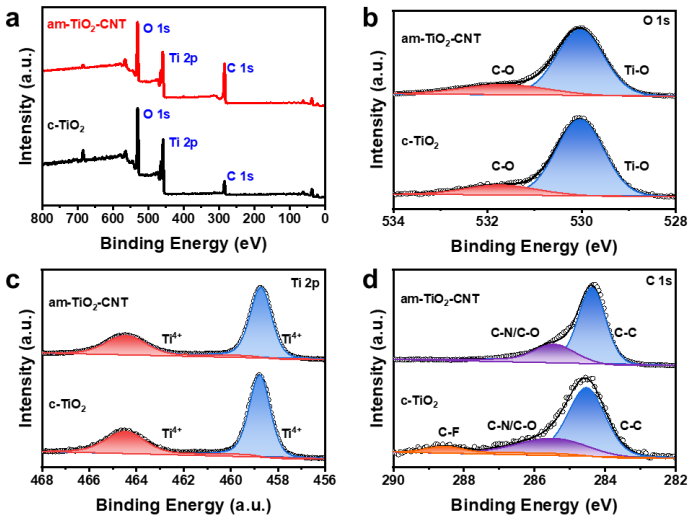

Fig. S8. (a) XPS survey spectra of c-TiO_2 NPs and am-TiO_2-CNT. High-resolution XPS spectra of c-TiO_2 and am-TiO_2-CNT: (b) O 1s, (c) Ti 2p, and (d) C 1s.

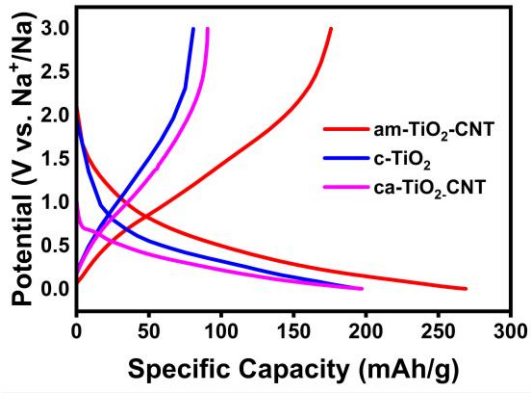

Fig. S9. GCD curves of various TiO_2-based electrodes at 500 mA/g.

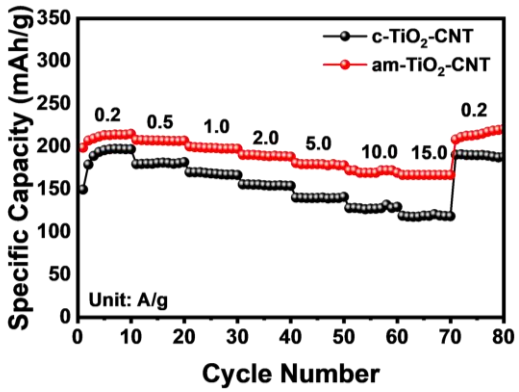

Fig. S10. Rate performances of am-TiO_2-CNT and c-TiO_2-CNT electrodes.

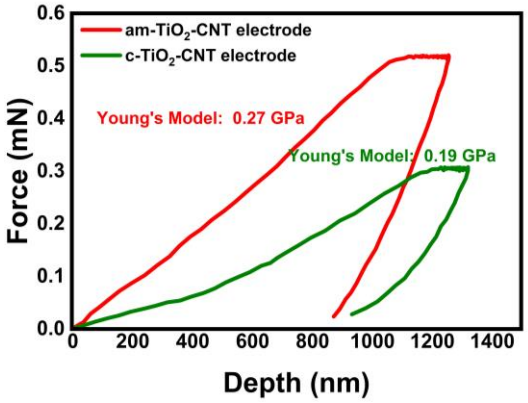

Fig. S11. Load-displacement curves of the am-TiO_2-CNT and c-TiO_2-CNT electrodes, respectively.

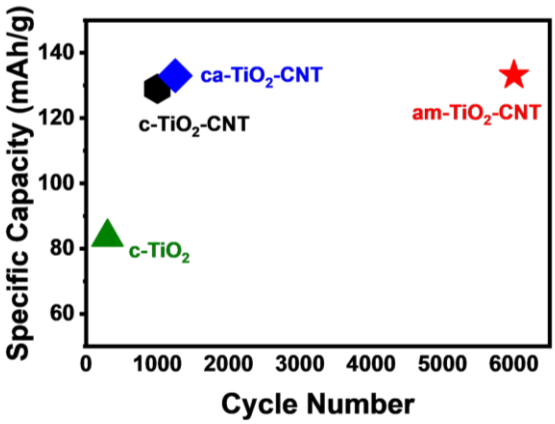

Fig. S12. Comparison of the cycling performances of am-TiO_2-CNT, ca-TiO_2-CNT, c-TiO_2, and c-TiO_2-CNT at 10 A/g.

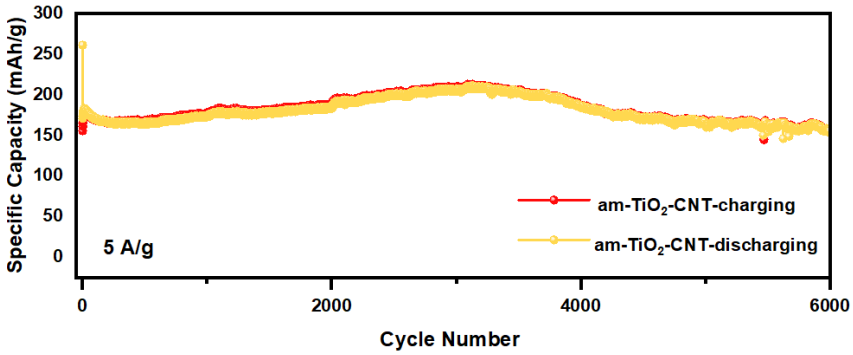

Fig. S13. Long-term cycling performance of the am-TiO_2-CNT electrode at the current rate of 5 A/g.

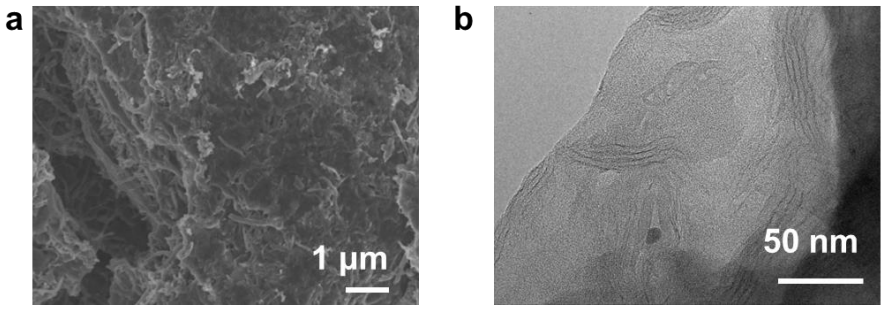

Fig. S14. (a) SEM and (b) TEM images of am-TiO_2-CNT electrodes after 6000 cycles at 10 A/g.

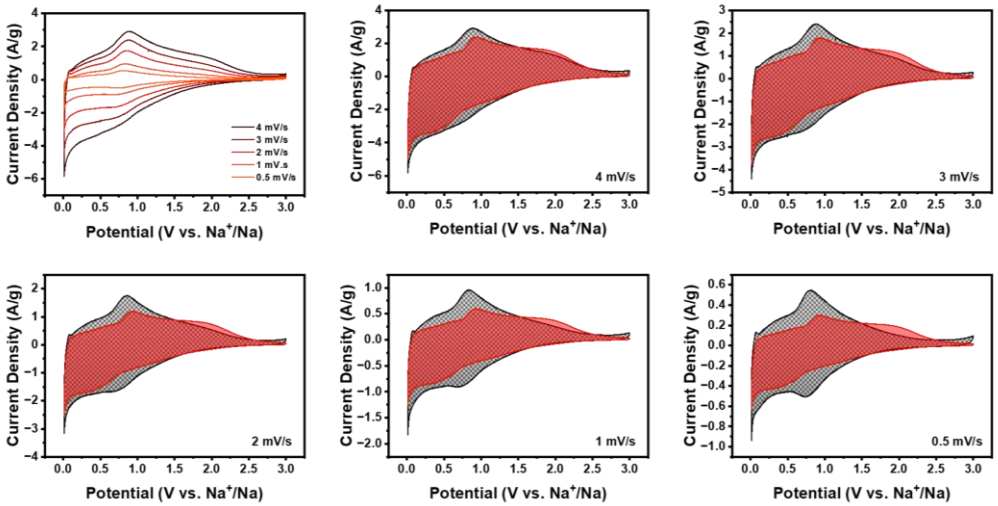

Fig. S15. CV curves of the am-TiO_2-CNT electrode at different scan rates and the contribution of the capacity.

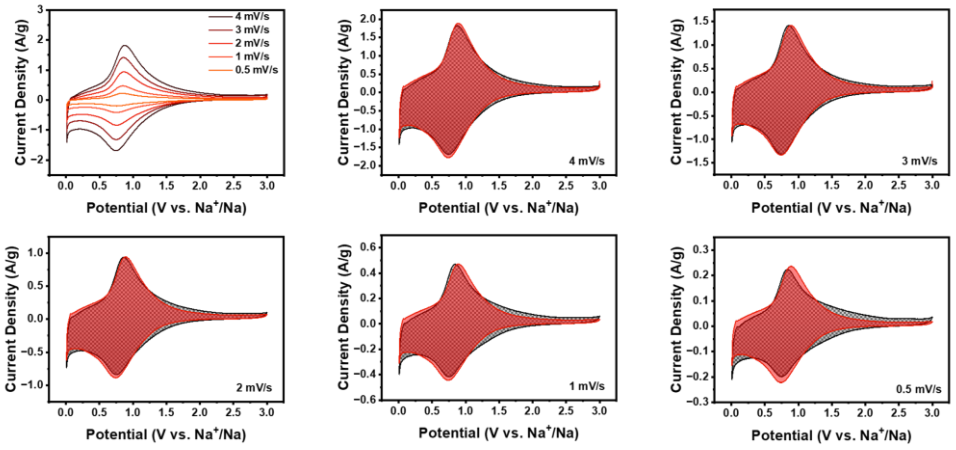

Fig. S16. CV curves of the c-TiO_2 electrode at different scan rates and the contribution of the capacity.

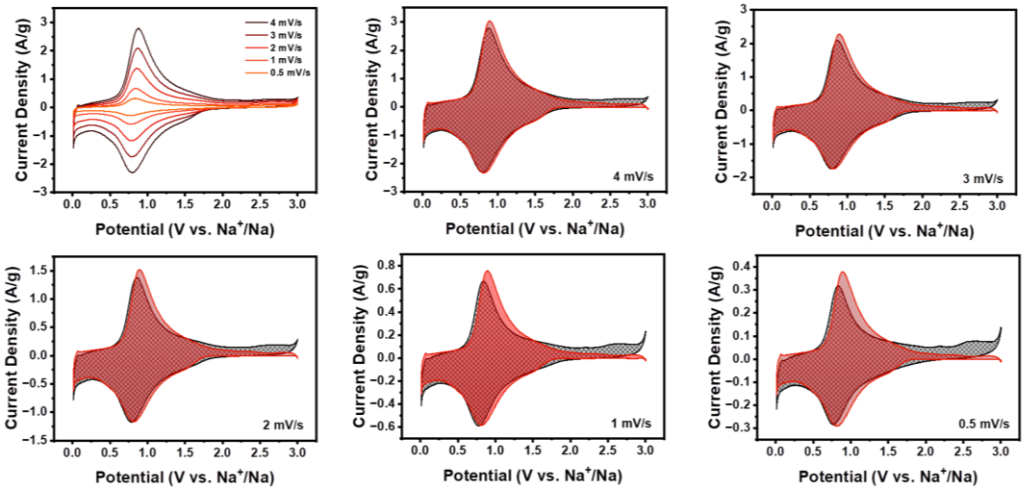

Fig. S17. CV curves of the ca-TiO_2-CNT electrode at different scan rates and the contribution of the capacity.

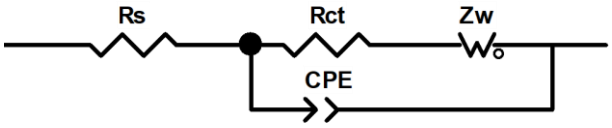

Fig. S18. Equivalent circuit of am-TiO_2-CNT, c-TiO_2, and ca-TiO_2-CNT in SIBs

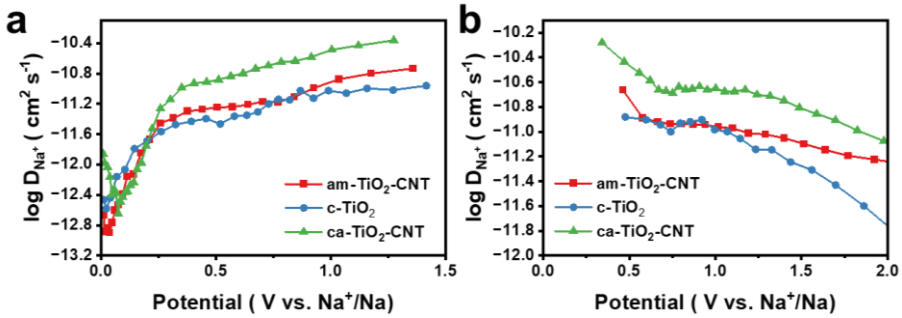

Fig. S19. Calculated sodium-ion diffusion coefficients (D_{Na^+}) in the (a) discharging and (b) charging processes for am-TiO_2-CNT, ca-TiO_2-CNT, and c-TiO_2 electrodes based on the GITT measurements.

GITT measurements corroborated the lower D_{Na^+} of am-TiO_2-CNT compared to ca-TiO_2-CNT. This discrepancy stems from fundamentally different sodium storage behaviors between crystalline and amorphous structures. For crystalline TiO_2, sodium storage is primarily confined to surface layers (3-5 nm in depth), artificially inflating the value since only surface reactions contribute. In contrast, Na^+ storage occurs throughout the bulk of am-TiO_2 NSs due to their atomically disordered structure. While this leads to longer diffusion pathways (and thus numerically lower D_{Na^+}), it reflects full active-material utilization rather than surface-limited kinetics.

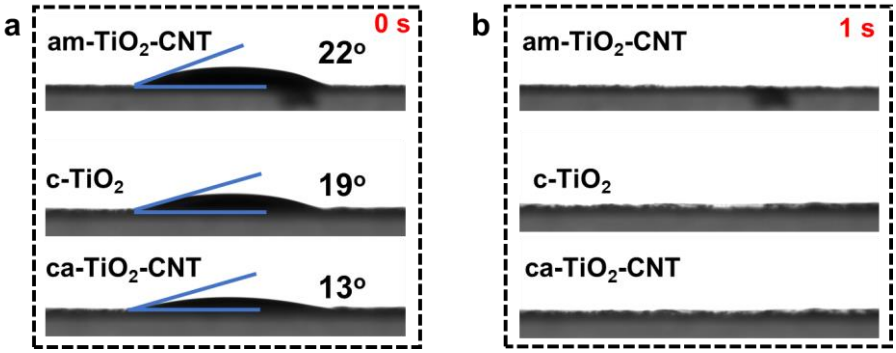

Fig. S20. The contact-test of the am-TiO_2-CNT, c-TiO_2 and ca-TiO_2-CNT electrodes at different time intervals: (a) 0 s; (b) 1 s.

In the case of c-TiO_2 NPs and ca-TiO_2-CNT electrodes, the random stacking of NPs generates numerous cracks within the electrodes, enhancing electrolyte penetration. In contrast, the lamellar arrangement of am-TiO_2 NSs, combined with their large surface area, hinders the complete wetting of electrodes. Nonetheless, the highly-accessible superstructure allowed am-TiO_2-CNT to achieve rapid electrolyte permeation (<1 s), thereby minimizing its impact on overall electrochemical performance.

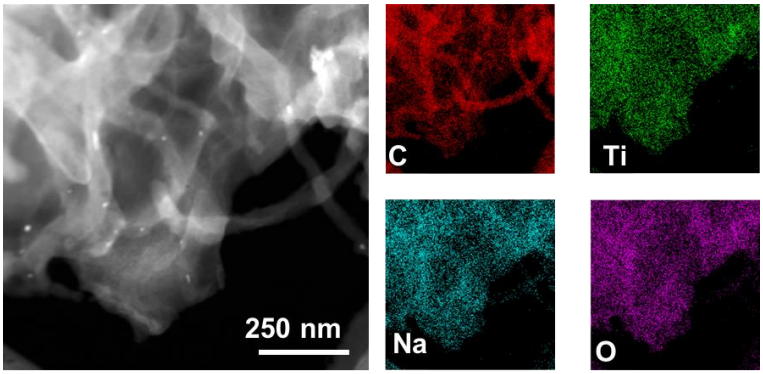

Fig. S21. STEM image and corresponding elemental mappings of the am-TiO_2-CNT electrode after the sodiation process, showing the uniform distribution of Na across the NSs.

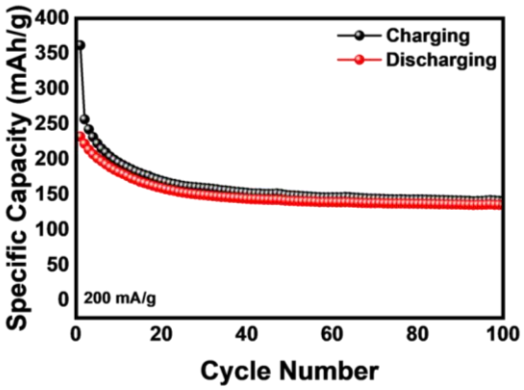

Fig. S22. Cycling performances of full-cells of $Na_3V_2(PO_4)_3$//am-TiO_2-CNT at 200 mA/g.

Table 1 Rate performance comparison between am-TiO_2-CNT and reported TiO_2-based anode materials for SIBs.

Electrode materials	**Current density (A/g)**	**Specific capacity (mAh/g)**	**Ref.**
NF-TiO_2	10.05	157.8	[4]
	16.75	148.7	
TiO_{2-x} tube	2.00	172.8	[5]
	5.00	153.8	
	10.00	134.6	
TiC_xN_{1-x}/N-TiO_2	3.35	173.7	[6]
CON-TiO_2-HS	3.00	168.9	[7]
	4.00	138.5	
	5.00	120.2	
GTN-OD	2.50	104.3	[8]
	5.00	89.0	
S-am-TiO_{2-x}/S-MXene	5.00	167.7	[9]
	10.00	153.2	
TiO_2/C-HPD	5.00	110.3	[10]
	10.00	92.4	
am-TiO_2-CNT	**5.00**	**179.3**	**This work**
	10.00	**169.3**	
	15.00	**166.7**	

Table 2 Cycling performance comparison between am-TiO_2-CNT and reported TiO_2-based anode materials for SIBs.

Electrode materials	Current density (A/g)	Cycling number	Specific capacity (mAh/g)	Ref.
S-am-TiO_{2-x}/S-MXene	10.00	10000	121.0	[9]
TiO_2/C-HPD	10.00	10000	84.1	[10]
TiO_2@TiO_{2-x}-P	10.00	5000	168.0	[11]
NS-TiO_2	3.35	2400	157.4	[12]
TiO_2/SCNT	3.35	1000	118.0	[13]
TiO_2-HS	5.00	4000	119.0	[14]
P-TiO_2	3.35	1000	141.0	[15]
a-TiO_{2-x}/r-TiO_{2-x}	3.35	4500	134.0	[16]
TiO_2-$TiOF_2$	0.50	2000	151.7	[17]
am-TiO_2-CNT	**5.00**	**6000**	**159.0**	**This work**
	10.00	**6000**	**133.2**	

Reference

1.X. Lyu, G. Wu, Z. Zheng, S. Xia, J. Xie, Y. Xia, P. Fan, R. Zhu, Y. Wang, D. Yang, T. Li and A. Dong, *ACS Nano*, 2024, **18**, 2219-2230.

2.M. Naguib, M. Kurtoglu, V. Presser, J. Lu, J. Niu, M. Heon, L. Hultman, Y. Gogotsi and M. W. Barsoum, *Advanced Materials*, 2011, **23**, 4248-4253.

3.Y. Ling, W. Li, B. Wang, W. Gan, C. Zhu, M. A. Brady and C. Wang, *RSC Advances*, 2016, **6**, 31037-31045.

4.D. Lv, D. Wang, N. Wang, H. Liu, S. Zhang, Y. Zhu, K. Song, J. Yang and Y. Qian, *J. Energy Chem.*, 2022, **68**, 104-112.

5.C. Wang, N. Cheng, Z. Bai, Q. Gu, F. Niu, X. Xu, J. Zhang, N. Wang, B. Ge, J. Yang, Y. Qian and S. Dou, *J. Energy Chem.*, 2023, **77**, 369-375.

6.Q. Cai, X. Li, E. Hu, Z. Wang, P. Lv, J. Zheng, K. Yu, W. Wei and K. K. Ostrikov, *Small*, 2022, **18**, e2200694.

7.M. Lee, M. S. Kim, J. M. Oh, J. K. Park and S. M. Paek, *ACS Nano*, 2023, **17**, 3019-3036.

8.W. Wang, M. Wu, P. Han, Y. Liu, L. He, Q. Huang, J. Wang, W. Yan, L. Fu and Y. Wu,

ACS Appl. Mater. & Inter., 2018, **11**, 3061-3069.

9.C. Lu, X. Li, R. Liu, H. J. Niu, Q. Wang, T. Xiao, J. Liu, H. Wang and W. Zhou, *Adv. Funct. Materi.*, 2023, **33**, 2215228.

10.D. Chen, Y. Wu, Z. Huang and J. Chen, *Nano-Micro Letters*, 2022, **14**, 156.

11.Q. Gan, H. He, Y. Zhu, Z. Wang, N. Qin, S. Gu, Z. Li, W. Luo and Z. Lu, *ACS Nano*, 2019, **13**, 9247-9258.

12. M. Fan, Z. Lin, P. Zhang, X. Ma, K. Wu, M. Liu and X. Xiong, *Adv. Energy Mater.*, 2020, **11**, 2003037.

13.S. Luo, T. Yuan, L. Soule, J. Ruan, Y. Zhao, D. Sun, J. Yang, M. Liu and S. Zheng, *Adv. Funct. Mater.*, 2019, **30**, 1908309.

14.X. Xu, B. Chen, J. Hu, B. Sun, X. Liang, N. Li, S. A. Yang, H. Zhang, W. Huang and T. Yu, *Adv. Mater.*, 2019, **31**, 1904589.

15.J. Ni, S. Fu, Y. Yuan, L. Ma, Y. Jiang, L. Li and J. Lu, *Adv Mater*, 2018, **30**, 1704337.

16.Y. Wu, Y. Jiang, J. Shi, L. Gu and Y. Yu, *Small*, 2017, **13**, 1700129.

17.S. Guan, Q. Fan, Z. Shen, Y. Zhao, Y. Sun and Z. Shi, *J. Mater. Chem. A*, 2021, **9**, 5720-5729.